Tribology International 166 (2022) 107346

Contents lists available at ScienceDirect

Tribology International

journal homepage: www.elsevier.com/locate/triboint

Design of smart lubricants using the inverse ferrofluid approach

R. Sahoo [a], P. Ussa-Aldana [b], D. Lancon [b], F. Rondelez [b,c], J.R. Morillas [a], R. Hidalgo-Alvarez [a], J. de Vicente [a,*]

[a] Department of Applied Physics and Excellence Research Unit 'Modeling Nature' (MNat), Faculty of Sciences, University of Granada, C/Fuentenueva s/n, 18071 Granada, Spain

[b] Totalenergies, Solaize Researcher Center, BP22–69360, Cedex, France

[c] Laboratoire des Fluides Complexes et Réservoirs, Université de Pau et des Pays de l'Adour, E2S UPPA, CNRS, TOTAL, UMR 5150, BP 1155, 64013 Pau, France

ARTICLE INFO

Keywords:
Lubrication
Magnetic fields
Magnetorheology
Inverse ferrofluids
High shear lubrication
Negative magnetophoresis

ABSTRACT

A new formulation is proposed to lubricate tribopairs in extreme conditions where the amount of lubricant is small and the lubricating region highly confined. It is composed of non-magnetic solid lubricants dispersed in an oil-based ferrofluid. When this inverse ferrofluid (IFF) is magnetically activated, the lubricant particles are subjected to magnetophoretic forces. By using appropriate magnetic field gradients, they can be driven to the region of interest and thus control the friction locally. The rheological and tribological performances of three IFF formulations are evaluated in several conditions of applied magnetic field strength and shear flow rates.

1. Introduction

It is a well-known fact that the use of nanofluids, dispersions of nanoparticles in a carrier, as lubricants entails several advantages in their tribological performance [1]. Different types of nanoparticles have been added to improve the lubricant anti-wear properties (friction coefficient, wear scar diameter, wear rate) as well as their thermal properties (heat transfer coefficient, viscosity) [2,3]. The latter properties eventually allow operating in a wider temperature range (by lowering/increasing the lubricant pouring/flash point) and a better control of the system temperature [4,5].

From an experimental point of view, it is commonly reported that tribological attributes are optimal for a given nanoparticle concentration while thermal properties are enhanced as concentration increases [2,3]. However, high-concentration nanofluids also imply undesired cons such as nanoparticle aggregation and sedimentation in (too) short time scales what affect negatively their tribological performance [6,7]. A possible solution to these shortcomings could be the synthesis of dilute lubricant nanofluids whose concentration would be tuned locally so that it reaches the required value, and thus the targeted tribological properties, only in the system areas where wear takes place. Such a "smart" lubricant has already been conceived using, for example, the so-called magnetorheological (MR) fluids under external magnetic fields [8].

MR fluids consist in dispersions of micron-sized magnetic multidomain particles (typically carbonyl iron) in a non-magnetic liquid carrier [9]. In the absence of external magnetic fields, they behave as Newtonian fluids with a shear rate-independent viscosity. However, in the presence of sufficiently strong magnetic fields, the particles reorganize according to the magnetic field lines and finally aggregate to form strong field-directed structures. As a result, the dispersions exhibit an apparent yield stress and viscoelasticity [10–12]. In the last decade, the tribological properties of MR fluids have been extensively documented [13–15]. In most cases, they do not exhibit appropriate lubricating properties because of their large particle size and concentration (above 10 vol%) [14]. In fact, they are frequently used in polishing applications, when doped with abrasive particles [16,17].

By reducing the particle size of the previous systems, one gets a ferrofluid (FF). These are semi-dilute dispersions (below 10 vol%) of nano-sized magnetic monodomain particles (typically magnetite) in liquid carriers [18]. In contrast to MR fluids, they exhibit very good lubricating properties because their particle size is significantly lower [19,20]. Nevertheless, in FFs Brownian motion plays a significant role and typically avoids control over particle aggregation/reorganization, giving rise to a homogeneous particle distribution within the FF, even in the presence of a magnetic field.

Besides MR fluid and FF families, a third main group of magnetic suspensions has been traditionally considered as sharing some of the main advantages of the formers. They are the inverse ferrofluids (IFFs),

* Corresponding author.
E-mail address: jvicente@ugr.es (J. de Vicente).

https://doi.org/10.1016/j.triboint.2021.107346
Received 21 September 2021; Received in revised form 31 October 2021; Accepted 3 November 2021
Available online 15 November 2021

dispersions of non-magnetic particles (typically silica or polystyrene) in a ferrofluid [21–23]. On the one hand, they are interesting systems for magnetorheology because they are governed by dipolar magnetostatic interactions like the FFs. On the other hand, the non-magnetic particle size can be of the same order as in MR fluids, reducing the importance of Brownian motion and allowing particle reorganization according to magnetic field lines. What is more, the non-magnetic particles can be chosen to show convenient properties such as monodispersity [24–26] or, of interest in this work, good lubricity. IFF rheological properties have been extensively investigated [22,26–28] but their tribological behaviour is yet unknown.

In this manuscript, novel IFFs are formulated in which the non-magnetic particles are for the first-time solid lubricants (e.g., MoS_2, PTFE or SiO_2). When such particles are dispersed in a FF, it is possible to alter their concentration locally by using magnetic fields. The main objective of this manuscript is to elucidate if an external magnetic field of proper strength and gradient is capable to tune the rheological and tribological performances of solid lubricant-based IFFs at specific positions. With this in mind, one can hope to apply the method to narrow spaces and thus to control friction in moving mechanical parts.

2. Background

The rheological behaviour of IFFs can be understood by using the mean magnetisation (MM) approximation [24,29] in which each non-magnetic particle is viewed as a magnetic dipole placed at its centre. Hence, the interaction force between two particles is treated as a dipole-dipole interaction.

In the presence of a homogeneous magnetic field, H_o, three major interactions have to be considered, namely magnetic, hydrodynamic and thermal (i.e. Brownian motion). Two independent dimensionless numbers are generally introduced in the equations: The Mason number, Mn, and the Lambda ratio, λ. Mn is the ratio between hydrodynamic and magnetic interactions and λ is the ratio between magnetic and thermal interactions [29–32]. If the particle radius, R, is large as in MR fluids, $\lambda >> 1$ since it scales as R^3, and therefore only the particle volume fraction ϕ and Mn are needed in the description of the rheological behaviour [33].

In its most general form, valid for both low and high magnetic fields [29], Mn is expressed as:

$$\mathrm{Mn} = \frac{72\eta_c\dot{\gamma}}{\mu_o\mu_{cr}\langle M_p\rangle^2} \tag{1}$$

where η_c denotes the viscosity of the continuous phase, $\dot{\gamma}$ the magnitude of the shear rate tensor, μ_o the magnetic permeability of the vacuum, μ_{cr} the relative magnetic permeability of the continuous medium and $\langle M_p\rangle$ the mean magnetisation of the particles.

For low fields, in the linear regime,

$$\langle M_p\rangle = 3\beta H_o \tag{2}$$

where $\beta = \left(\mu_{pr} - \mu_{cr}\right) \Big/ \left(\mu_{pr} + 2\mu_{cr}\right)$ is the contrast factor and μ_{pr} is the relative magnetic permeability of the particles.

Recent theoretical developments, simulations, and experiments, have demonstrated that the steady shear viscosity, η, of MR fluids is dictated by a Casson plastic equation [34]:

$$\frac{\eta}{\eta_\infty} = 1 + \left(\frac{\mathrm{Mn}}{\mathrm{Mn}^*}\right)^{-1} + 2\left(\frac{\mathrm{Mn}}{\mathrm{Mn}^*}\right)^{-1/2} \tag{3}$$

where Mn^* is the critical Mason number and η_∞ is the high shear viscosity. The dependence on ϕ is solely contained in Mn^* [29].

If the applied magnetic field is not homogeneous, $\vec{H}$, each dipole induced in the dispersed particles will interact with the field gradient giving rise to another force, called the magnetophoretic force:

$$\vec{f} = \mu_o\mu_{cr}V_p\langle\vec{M}_p\rangle\bullet\nabla\vec{\mathrm{H}} = \frac{3}{2}\mu_o\mu_{cr}\mathrm{V_p}\beta\nabla\mathrm{H}^2 \tag{4}$$

where V_p is the particle volume. Since $\mu_{pr} < \mu_{cr}$ by definition of IFFs, β is always negative and the magnetophoretic force, $\vec{f}$, will be opposite to the magnetic field gradient. Therefore, the dispersed non-magnetic particles will be attracted to regions where H^2 is minimum.

3. Materials and methods

3.1. Non-magnetic particles

Molybdenum disulphide (MoS_2) particles were obtained from an external supplier (US Nanomaterials, reference # 1317–33–5) and used as received. Polytetrafluoroethylene (PTFE) particles were purchased from Dupont (Spain). Silica (SiO_2) particles were fabricated by following Stöber method [35] with minor modifications described in Ramos et al. [26]. Absolute ethanol, ammonia and water were first mixed in a 500 mL reactor vessel. Then, 0.2 M tetraethylethoxysilane was added up to a final volume of 500 mL and the reaction mixture was stirred at room temperature for one day. The molar concentration ratio was water/-ammonia = 2.49/1.06. Silica particles were recovered by centrifugation at 12,000 g and 15,000 rpm during 15 min and washed by repeated dispersions in ethanol three times. The sediment was dried in a vacuum oven at 80 °C for 24 h.

The particle sizes were measured by several methods: dynamic light scattering (Zetasizer-Nano-ZS, Malvern Instruments, UK), scanning electron microscopy (SEM-Quanta 400) and transmission electron microscopy (TEM-Libra 120).

3.2. Ferrofluid: (FF)

The FF employed in this work was a dispersion of magnetite nanoparticles in polyalphaolefin (PAO). PAO was purchased from Ineos Europe Limited (Belgium) and its viscosity was 8 mPa·s at room temperature. More detailed information on the PAO physicochemical properties can be found in the Supplementary Material.

The magnetite nanoparticles were fabricated by the coprecipitation method [36]. Firstly, 18 g of $FeSO_4{\cdot}7H_2O$ and 34 g of $FeCl_3{\cdot}6H_2O$ are weighed in a container and dissolved in 375 mL of water under vigorous mechanical stirring. This step is followed by the successive additions of 88 mL of ammonia solution (30%) and 8 g of oleic acid. The solution is then left for 1 h at room temperature (25 °C). Once everything is properly mixed, the temperature is increased to 95 °C using a thermostatic bath to convert iron hydroxide into magnetite. When the temperature reaches 95 °C, the suspension temperature is decreased to room temperature by dipping the container in a water bath. Next, the solution is acidified to pH 5 by drop addition of a HNO_3 solution (35%) to enhance the adsorption of oleate ions onto the magnetite particles. At this point, the particles clump together due to the hydrophobic oleate layer [37]. The precipitate is washed four times with water to remove the salts. Additional washing with acetone helps to remove water and non-adsorbed oleic acid.

To obtain the FF, the magnetic precipitate is then mixed with 170 mL of PAO. The suspension is heated to 40–50 °C under mechanical stirring to remove the acetone, sonicated for 20 min and centrifuged at 12,000 g and 12,000 rpm for 60 min to remove the largest aggregates.

3.3. Inverse ferrofluid: (IFF)

The IFFs were prepared by dispersing different volume fractions (ϕ = 1, 2, 5 and 10 vol%) of the non-magnetic particles in the PAO-based FF. In terms of weight fractions, these concentrations correspond to: 5.0, 9.7, 21.6 and 36.8 wt% (MoS_2); 2.2, 4.4, 10.7 and 20.2 wt% (PTFE); 1.9, 3.9, 9.4 and 17.9 wt% (SiO_2). The particles were mixed manually with a

glass rod, then vortexed for 10 min and finally sonicated for 10–15 min. For the concentrations investigated in this work, we did not observe settling of magnetite particles and the ferrofluid kept the same dark/brownish colour since it was prepared (see the Supplementary Material). On the contrary, aggregation was clearly observed for concentrations much exceeding 10 vol%.

3.4. Rheometry

A MCR-501 magneto-rheometer (Anton Paar) with a MRD70/1 T magneto-cell [38] was used in parallel plate configuration (20 mm diameter, 0.3 mm gap) for the rheological investigation of the IFFs at concentrations $\phi = 1$, 2, 5 and 10 vol%. The samples were first sheared at a constant rim shear rate of 100 s^{-1} during 1 min. Then, the shear rate was gradually increased from 0.1 s^{-1} to 10^3 s^{-1}, in a strain-controlled fashion. The acquisition time of each data point was 10 s. The applied magnetic fields were from 0 to 146 kA/m. In this range, their homogeneity within the sample volume is rather good and field gradients are negligible. All measurements were carried out at room temperature (25 °C).

3.5. Tribometry

A MCR-302 tribometer (Anton Paar) with a ball-on-three plates geometry in steel-steel contacts (AISI 316) was used for these experiments. The ball (radius $R = 0.25$ in. $= 6.35 \times 10^{-3}$ m) was purchased from STL (UK) while the plates were parallelepipeds (length 16 mm, width 6 mm and thickness 2 mm) cut from large sheets purchased from Goodfellow (UK). In the experiments, the ball was attached to the upper shaft and rotated at a given sliding speed V under a normal force F_N while the plates were fixed in a holder. This arrangement provides three stationary sliding point contacts. For more details on the tribometer we refer to Shahrivar et al. [14].

To study the influence of the magnetic field on the tribological performance of the IFFs, two permanent magnets (W-01-N, Webcraft GmbH/ Supermagnete) were placed under the steel plates as sketched in Fig. 1a, just below the point contact. The magnets were cubes of 1 mm edge and 1.1×10^6 A/m of remanent magnetization. They were embedded in a polylactic acid (PLA) matrix manufactured by using a 3D printer (Ultimaker 3). The matrix had the appropriate dimensions to perfectly fit within the plates' holders: its length and width were the same as the steel plates, but its thickness was 1 mm only whereas the steel plate thickness was 2 mm. The magnet orientations were chosen in order to create a minimum of the magnetic field in the point contact region (see 6.2.1 for a detailed explanation). In this way, the magnetophoretic force experienced by the non-magnetic particles present in the IFF traps them in the point contact.

3.6. Finite element method calculations

Maxwell equations were solved using the Finite Element Method (COMSOL Multiphysics) to compute the magnetic field distribution around the point contact.

In a typical simulation, the two magnets are placed in the centre of a computational box (see Fig. 1b). The 2 mm-thick domain above the magnets that corresponds exactly to the steel plate thickness, is defined as the FF or IFF domain. This is regarded as a magnetic continuum with a constitutive equation given by the FF experimental magnetisation curve (see Fig. 3d). The magnetic behaviour of the permanent magnets is defined in our model by imposing the magnitude and direction of their remanent magnetisation. The rest of the computational box has the permeability of the air since there is no other magnetic material in the experimental setup.

The computational box size (cube of 20 mm edge) was chosen in order not to affect the magnetic field distribution near the point contact. At the boundary walls, the normal component of the magnetic field is imposed to be zero. Finally, the box is meshed with elements of different sizes depending on their proximity to the point contact. Near this point and the magnets, the elements have a typical edge smaller than 0.2 mm while they increase to 1.6 mm as they get closer to the boundaries of the computational box.

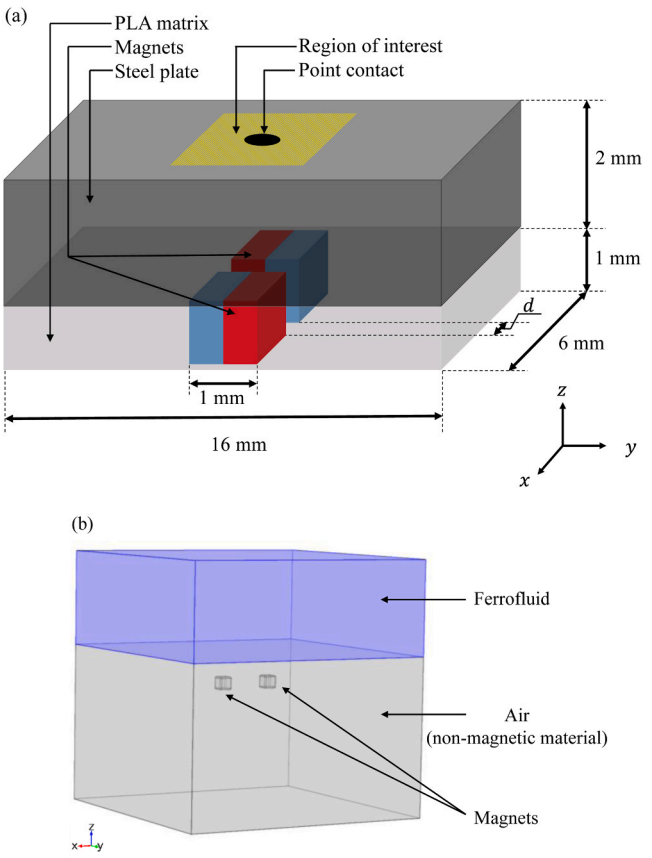

Fig. 1. (a) Schematic diagram of the steel-steel plate contact. The point contact on the steel plate is plotted with a black circle. The two magnets below (red/blue part stands for positive/negative pole) are embedded in a PLA matrix so that the total thickness (3 mm) fits in the holder. The distance between the two cubic magnets is $d =$ 3 mm. The yellow stripped square denotes the 3.5×3.5 mm^2 region where the gradient of the magnetic field squared is computed. (b) Computational box where the magnetic field is obtained using the Finite Element Method. The ferrofluid (blue region) is placed exactly 2 mm above the pair of magnets. The distance of 2 mm corresponds to the thickness of the steel plate. (For interpretation of the references to colour in this figure legend, the reader is referred to the web version of this article.)

The Finite Element Method provides the magnetic field flux, strength and magnetisation in the whole computational box. However, in this work we only focus on the magnetic field distribution and gradient in a two-dimensional region around the point contact, just above the two magnets on the steel plate. This region is sketched with a yellow stripped square in Fig. 1a. Its dimensions are 3.5 mm × 3.5 mm.

4. Characterization of the particles

4.1. Characterization of the non-magnetic particles

The MoS_2, SiO_2 and PTFE particles used in the formulation of the IFFs were dispersed in ethanol and observed with SEM and TEM for their size and shape characterization. Representative images are shown in Fig. 2. Whenever possible, 'ImageJ' software was used to compute the particle size histogram and the number-average diameter.

Fig. 2a shows two typical electron microscopy pictures of the MoS_2

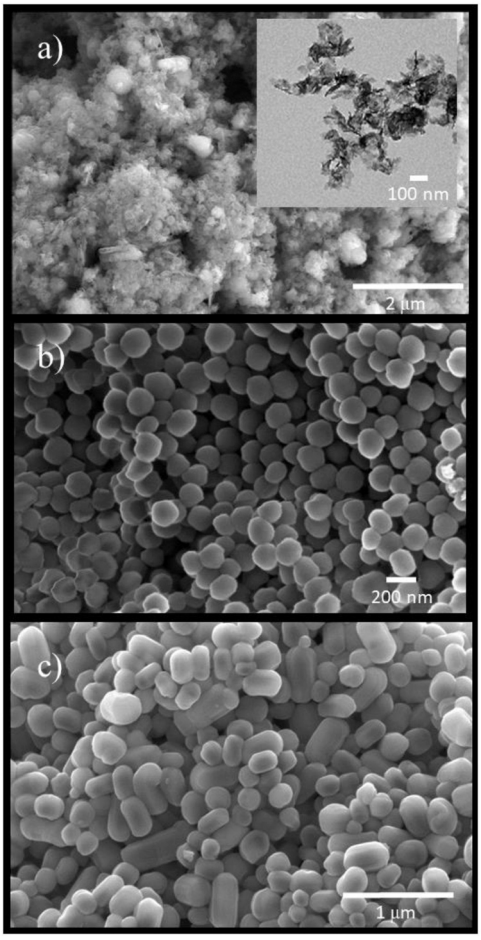

Fig. 2. Electron microscopy pictures of the lubricating particles used in this work. a) MoS_2 nanoparticles (inset corresponds to a detail with TEM), b) SiO_2 particles and c) PTFE particles.

particles used in this work. They appear plate-like shaped but, as they are clumped together, it was not possible to construct a particle size histogram from such images. According to the manufacturer, the MoS_2 particles are 135 nm in diameter with a roughly spherical shape. Dynamic light scattering on our samples yielded a hydrodynamic particle size of 240 ± 20 nm, in agreement with the fact that the particles are aggregated. The MoS_2 particles were also chemically analysed using EDX during SEM and TEM observations. The peaks confirmed that the sample composition was mostly MoS_2.

Fig. 2b shows that the particles of SiO_2 are much more monodisperse in size and shape than MoS_2. The particle size histogram gives a mean particle diameter of 188 nm and a standard deviation of 17 nm.

Fig. 2c shows that the particles of PTFE are elongated in shape and significantly longer than SiO_2 and MoS_2. Typical length is 330 nm, and the diameter is 190 nm.

Table 1
Mean particle size and standard deviation of the particles used in the formulation of the IFFs. Measurements for magnetite, SiO_2 and PTFE are made by SEM and TEM. Measurements for MoS_2 are made by Dynamic Light Scattering.

Particles	Mean particle size (nm)	Standard deviation (nm)	Polydispersity index
Magnetite	9.9	0.2	1.05
MoS_2	240	20	–
SiO_2	188	17	1.02
PTFE	Length: 330	90	1.07
	Diameter: 190	30	1.03

Table 1 summarizes the mean particle sizes and standard deviation results for all the particles used in this work. In practice, we expect the particles to be somehow aggregated in dispersion (see below).

4.2. Characterization of the magnetic particles

Fig. 3a and b show two pictures of the same batch of magnetite nanoparticles before and after addition of oleic acid. As expected, the aggregation is less severe in the presence of oleic acid, but they are still irregular in shape and polydisperse in size. The histogram of their diameter has been drawn in Fig. 3c: a log-normal fit yields an average diameter of 9.9 ± 0.2 nm. They are superparamagnetic (Fig. 3d): magnetisation is zero in the absence of field and the value at saturation is similar to those reported for other FFs [e.g., Ramos et al. [26]]. Comparing the saturation magnetisation of the FF (approx. 17 kA/m) with the saturation magnetisation for the magnetite [450 kA/m, [39]], the FF concentration should be approximately 20.4 wt% (3.8 vol%).

5. Magnetorheology results

5.1. Flow curves

Typical rheograms and viscosity curves, for a 21.6 wt% MoS_2-based IFF submitted to applied magnetic fields of different strengths, are shown in Fig. 4a and b, respectively. At low shear rates, changes by as much as 2 orders of magnitude (note the log-scale in the y-axis) for both the shear stress and shear viscosity are observed as the field strength is ramped from 0 to 146 kA/m. The rationale for such a behaviour is that gap-spanning structures are induced in the suspension by the magnetic field and they become stronger as the field is increased. These structures however are unstable under high shear and they disintegrate, causing shear-thinning. Consequently all curves start converging for shear rates approaching $10^3\ s^{-1}$.

It should be noted that shear-thinning also occurs in the absence of magnetic field (see the black squares in Fig. 4). It comes from the disintegration of the unavoidable particle aggregates formed during the suspension preparation process. Since these isolated aggregates do not span the measuring gap, the effect is 10^3 - 10^4 lower than with the magnetically-induced macrostructures.

5.2. Yield stress

Two different kinds of yield stresses, i.e., static and dynamic, can be extracted from Fig. 4a. On the one hand, the static yield stress ($\tau_{y,S}$) is the minimum stress required for the MR fluid to flow. It was obtained by extrapolating the shear stress at low shear rates (typically below $\dot{\gamma} \approx 0.1 s^{-1}$) in log-log representation. On the other hand, the dynamic yield stress ($\tau_{y,D}$) is the stress needed to continuously break the field-induced aggregates that partially reform in the presence of the magnetic field. Its value was deduced by fitting the high-shear rate (typically $\dot{\gamma} > 100 s^{-1}$) region of the rheogram to a Bingham plastic fluid equation in linear scales [30,40].

These yield stresses values are reported in Fig. 5 as a function of the magnetic field strength in the range 0–53 kA/m where the particle magnetisation is linear (see Fig. 3d). They can be fitted to a quadratic law, as predicted for small fields by the MM approximation [29]. This is also in line with existing experimental [41] and simulation data [42]. Of course, the yield stresses should level off at large field strengths, when the magnetisation of the magnetite particles used in the IFFs starts to saturate. This regime, however, was not observed here since it requires fields strengths well-above 100 kA/m for our PAO ferrofluid (see Fig. 3d).

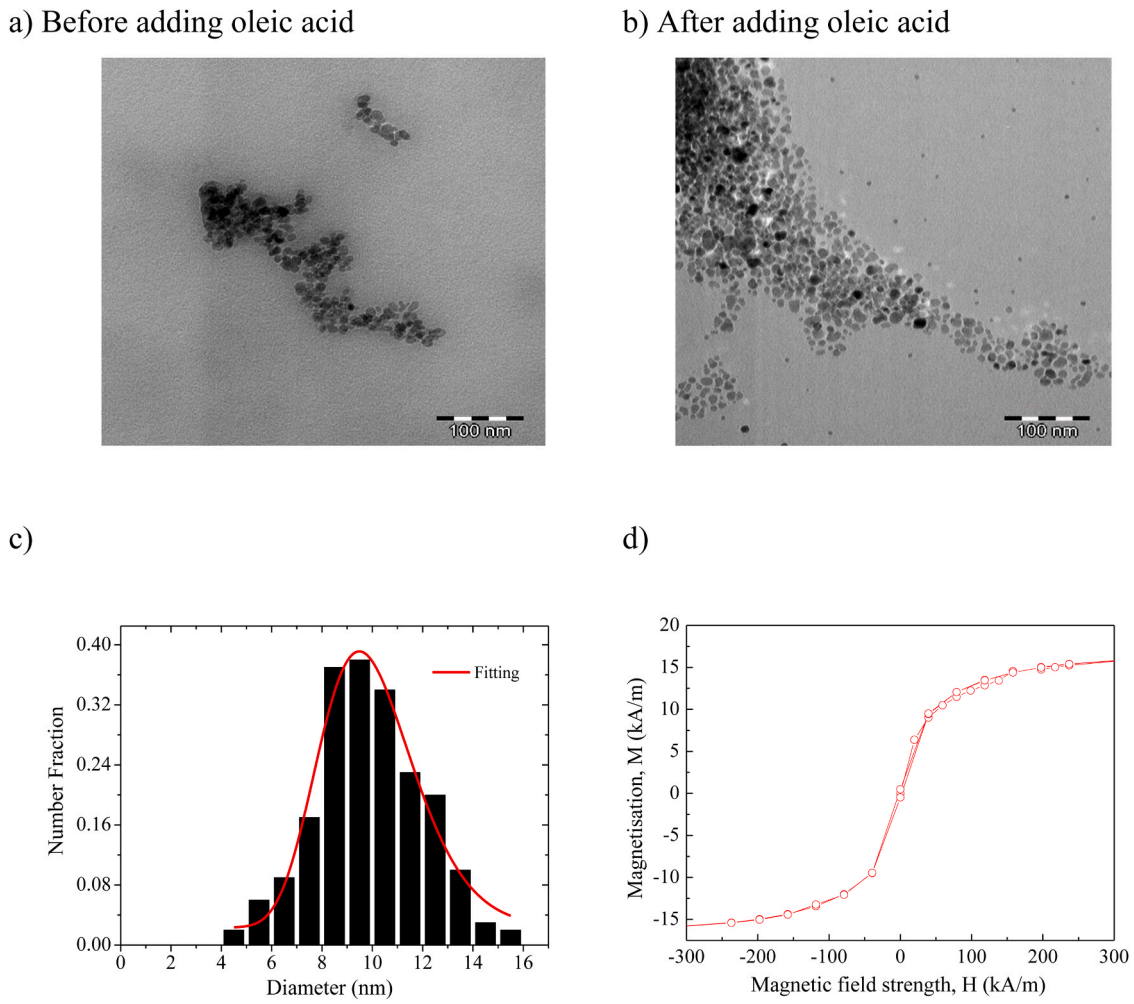

Fig. 3. TEM images of magnetite nanoparticles before (a) and after (b) adding oleic acid. c) Particle size histogram (number-average diameter) of the magnetite nanoparticles. The red line corresponds to the log-normal fitting curve. d) Magnetic hysteresis curve for the PAO ferrofluid at room temperature. (For interpretation of the references to colour in this figure legend, the reader is referred to the web version of this article.)

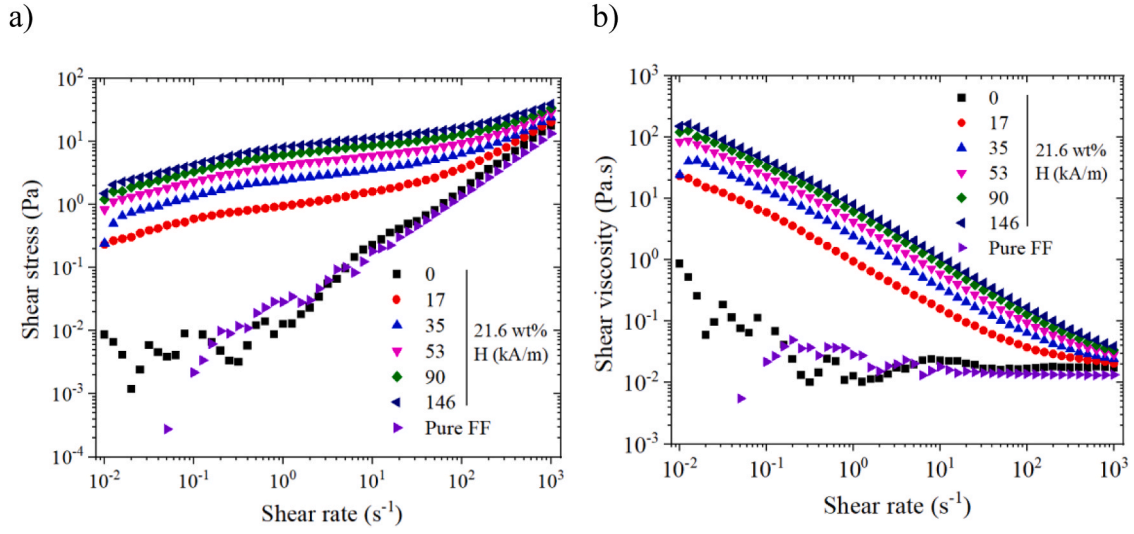

Fig. 4. a) Shear stress and b) Shear viscosity as a function of the shear rate for pure FF and an IFF containing 21.6 wt% concentration of MoS_2 nanoparticles under different external magnetic field strengths.

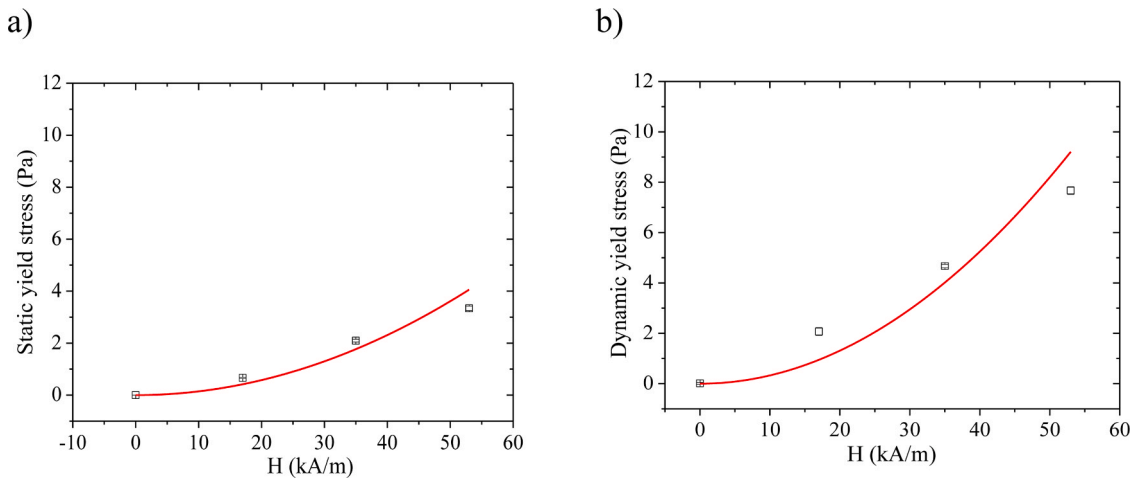

Fig. 5. a) Static and b) dynamic yield stress as a function of the magnetic field strength deduced from the rheograms reported in Fig. 4a. The red solid line is the best fit to a quadratic law. (For interpretation of the references to colour in this figure legend, the reader is referred to the web version of this article.)

5.3. Magnetorheological effect

We have plotted in Fig. 6a to c the dimensionless viscosity η/η_∞ as a function of the Mason number, Mn, for 3 different weight fractions of MoS_2 particles and 5 magnetic field strengths each time. The high shear viscosity, η_∞, is taken from the plateau region when Mn gets large. For the 36.8 wt% (10 vol%) sample, a plateau was not clearly observed. η_∞ was then calculated from the Quemada expression [29]: $\eta_\infty = \eta_c(1-\phi/\phi_m)^{-2}$, where η_c is the viscosity of the carrier fluid (i.e., the FF) taken from Fig. 4 and $\phi_m = 0.64$ is the maximum packing for perfectly monodisperse spheres.

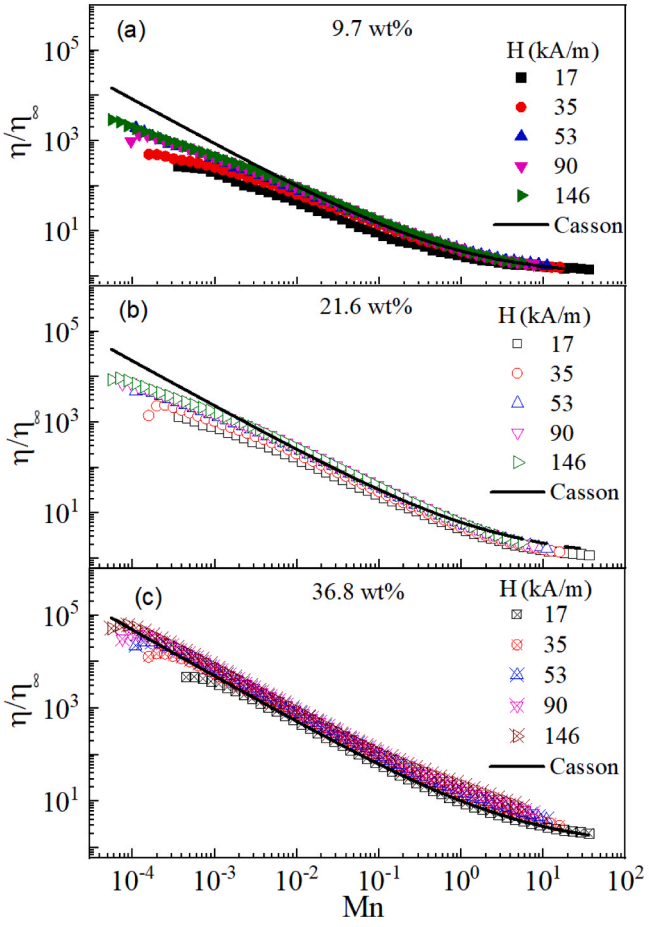

Fig. 6. Dimensionless viscosity, η/η_∞, as a function of the Mason number, Mn, at different magnetic field strengths for MoS_2-based IFFs with 9.7, 21.6 and 36.8 wt%. The solid lines correspond to the best fits to the Casson plastic model (Eq. 3).

For any given concentration, the curves at all magnetic field strengths superimpose on each other reasonably well. The Mn^* values were obtained by fitting the data of Fig. 6 to Eq. 3 and the Mn^*dependence on volume fraction, ϕ, is plotted in Fig. 7a. A least-square fit to a power law $Mn^* = a\phi^b$ yields $a = 0.43 \pm 0.02$ and $b = 1.04 \pm 0.08$. The essentially linear dependence of Mn on ϕ confirms the earlier result by Ruiz-Lopez et al. (2017) [29], $b = 1.03 \pm 0.10$, for an IFF loaded with large SiO_2 particles. Their $a = 0.24 \pm 0.08$ value was, however, slightly different. This is probably the effect of additional colloidal interactions, only present with the smaller MoS_2 particles.

In an attempt to see if the results could be condensed onto a master curve, independent of both field strength and particle concentration, the dimensionless viscosity has been plotted in Fig. 7b as a function of the reduced Mason number Mn/Mn^*. The solid line corresponds to the Casson plastic model (Eq. 3). The quality of the collapse is similar to others reported in the literature [29], but not perfect. Differences appear at low shear rates in agreement with an a value larger than expected. Other colloidal forces such as van der Waals and steric ones that have not been considered here certainly play a role when magnetic (at small fields) and hydrodynamics (at low shear rates) forces become negligible.

Fig. 7b is important because, once the critical Mason number Mn^* has been calculated, it allows anticipating the rheological behaviour of the IFF for any particular application. An example is given in Fig. 8 for a lubrication application in car engines, where the shear rate is typically 10^6 s^{-1}. Measurements of the viscosity show a dependence on concentration but not on the applied magnetic field. This result was logical since $Mn^*/Mn = \vartheta(10^{-7}) \ll 1$ and therefore $\eta/\eta_\infty \sim 1$. In more physical terms, hydrodynamic forces are dominant over magnetostatic interactions and the field-induced structures do not form. Any friction reduction would therefore require another mechanism than the MR effect. In the following, we will see that using field gradients and IFFs can be a solution for lubricating contacts.

6. Tribology

6.1. Tribology in the absence of magnetic fields

6.1.1. Stribeck curve

The Stribeck curves (i.e., plot of the friction coefficients versus

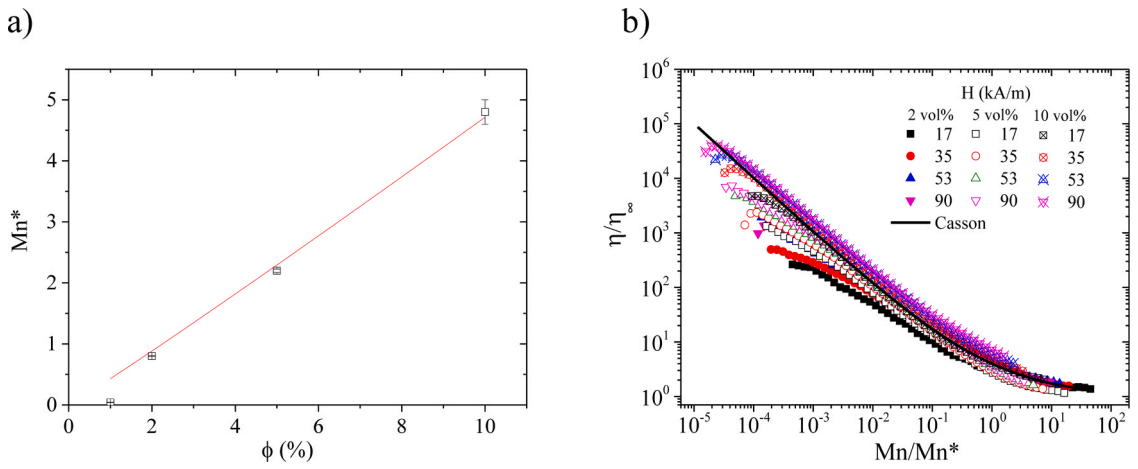

Fig. 7. a) Plot of the critical Mason number, Mn^*, as a function of the nanoparticle volume fraction, ϕ. Mn^* values were derived by fitting the dimensionless viscosity (η/η_∞) curves of Fig. 6 to the Casson model (Eq. 3). The red solid line corresponds to the best least-square fit to the equation $Mn^* = a\phi^b$ with $a = 0.43 \pm 0.02$ and $b = 1.04 \pm 0.08$. b) Dimensionless viscosity as a function of the reduced Mason number, Mn/Mn^*, at different field strengths and particle volume fractions. The black solid line corresponds to the Casson plastic model (Eq. 3). (For interpretation of the references to colour in this figure legend, the reader is referred to the web version of this article.)

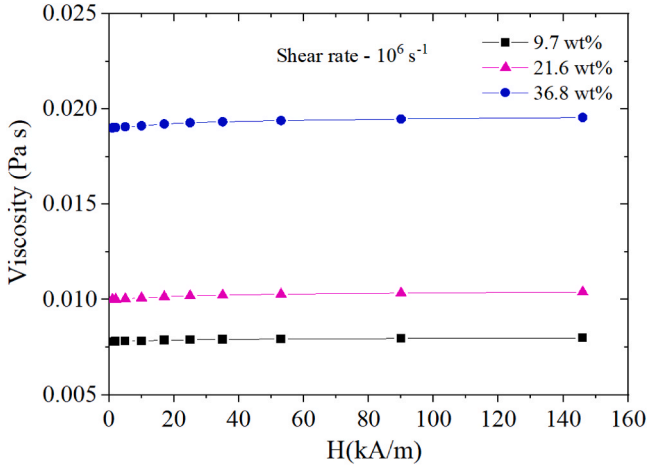

Fig. 8. Shear viscosity, η, as a function of magnetic field strength for MoS_2-based IFFs at three different concentrations (9.7, 21.6 and 36.8 wt%). Applied shear rate $\dot{\gamma} = 10^6$ s^{-1}.

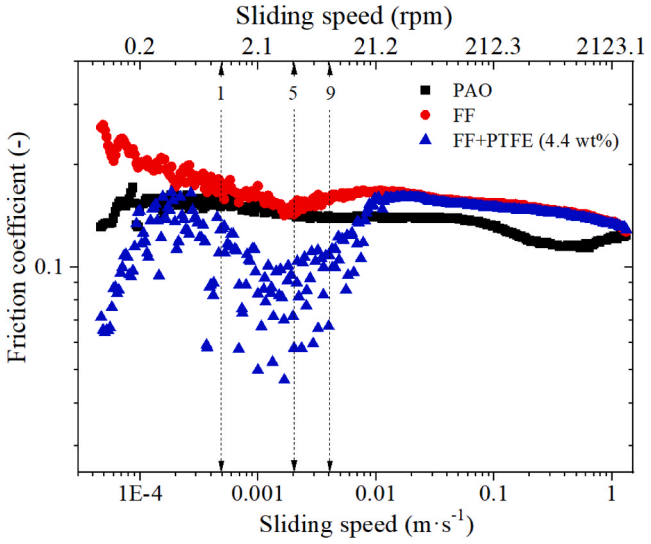

Fig. 9. Friction coefficient, μ, as a function of sliding speed V for PAO, FF and 4.4 wt% PTFE-based IFF. $F_N = 10$ N. No magnetic field applied. The vertical lines correspond to the sliding speeds investigated in Fig. 10.

sliding speeds) are drawn in Fig. 9 for PAO, FF and the 4.4 wt% PTFE-based IFF. The experimental conditions were identical for all three cases: maximum Hertzian contact pressure, $p_{max} \sim 10^8$ Pa, normal force, $F_N = 10$ *N*, and normal load, $w = 14$ *N*. The results demonstrate that the contact essentially operates in the boundary lubrication regime. The lowest friction levels are obtained at low sliding speeds (typically under 0.01 $m{\cdot}s^{-1}$) for the PTFE-based IFF, due to the action of the solid lubricant in the suspension and the ball bearing effect [43]. The measured values in this case are close to the resolution of the tribometer (0.1 μNm), which explains the large scatter observed for the friction coefficient data.

At this point it is important to remark that the particle concentration (4.4 wt%) and normal force (10 N) had to be chosen carefully. The results are not shown here for sake of brevity, but we did check that, on one side, smaller particle concentrations of PTFE do not exhibit enough changes with respect to the PAO and FF reference fluids, and, on the opposite side, concentrations larger than 4.4 wt% lead to a friction increase due to the onset of lubricant starvation. A similar observation was reported by Shahrivar et al. [14]. In addition, we have observed that the normal force of 10 N was optimum in our case. Larger values do not bring substantial differences in the experimental results and smaller ones give unevenly-loaded point contacts.

6.1.2. *Time dependent friction tests*

Since we have seen that the contacts operate in the boundary lubrication regime, the influence of time on the frictional response has been investigated, focusing on slow sliding speeds where the flow is uniform, and starvation does not occur.

Fig. 10a to c shows in black squares the time dependence of the friction coefficient in the absence of field for the 4.4 wt% PTFE-based IFF sample. Three different sliding speeds have been tested, namely 1 rpm, 5 rpm and 9 rpm. The normal force F_N was 10 *N* in all cases. Note that the red circles in Fig. 10 present the same data but now with a magnetic field gradient applied (Magnetic field strength $H = 180$ $A{\cdot}m^{-1}$; $\nabla H^2 = 10^9$ $A^2{\cdot}m^{-3}$ and $\nabla H = 2.6 \times 10^6$ $A{\cdot}m^{-2}$). The results will be discussed in Section 6.2.2.

For the 1 rpm sliding speed (Fig. 10a) the friction coefficient decreases monotonically from 0.16 to 0.04 over the 50 min of the

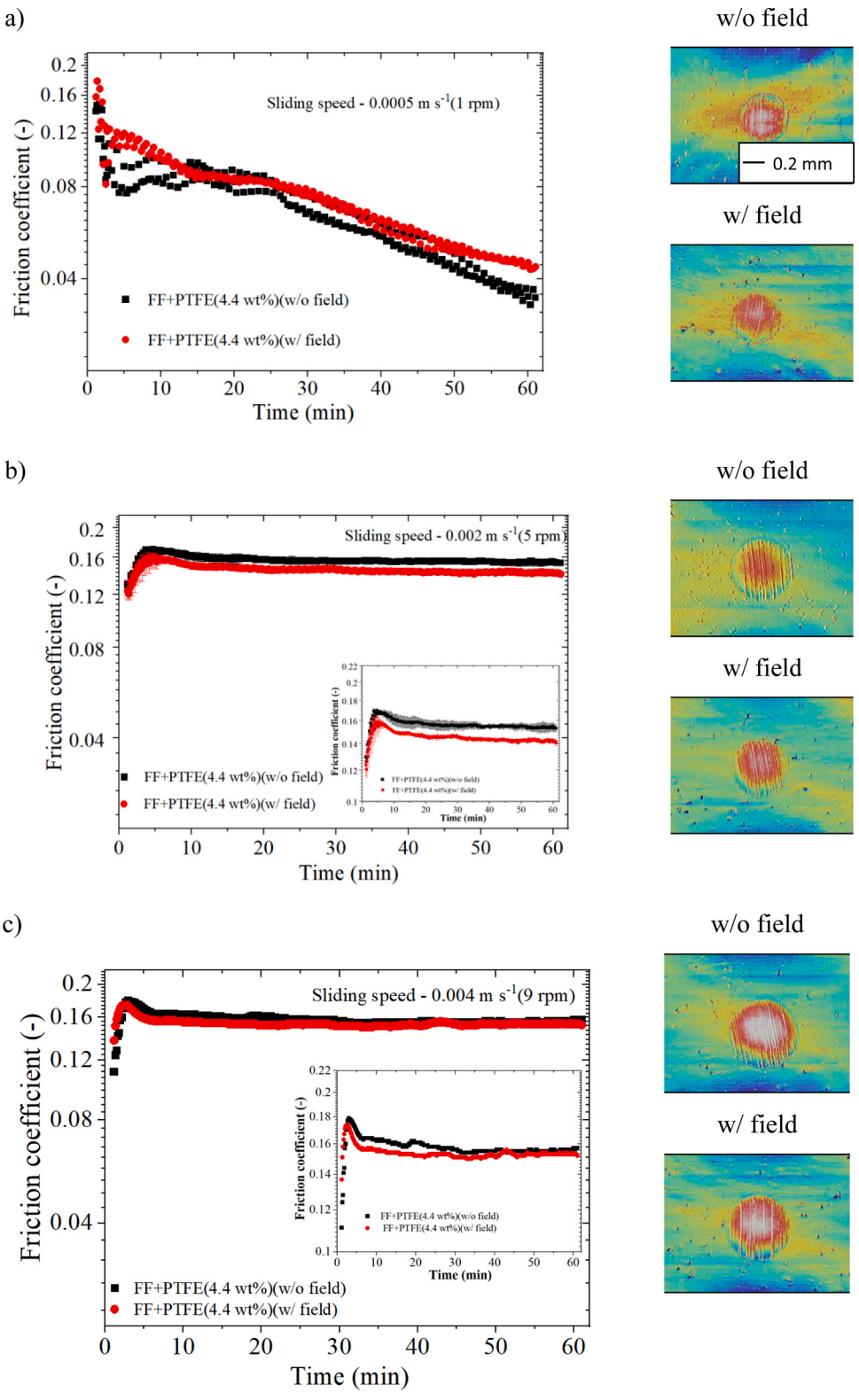

Fig. 10. Friction coefficient, μ, as a function of time, for the 4.4 wt% PTFE-based IFF at three different sliding speeds, V, and with (without) magnetic field. a) $V = 1$ rpm $= 0.0005$ m s^{-1}. b) $V = 5$ rpm $= 0.002$ m s^{-1}. c) $V = 9$ rpm $= 0.004$ m s^{-1}. $F_N = 10$ N in all cases. Black solid squares: without field. Red solid circles: with field (Magnetic field strength H= 180 A·m^{-1}; $\nabla H^2 = 10^9$ A^2·m^{-3} and $\nabla H = 2.6 \times 10^6$ A·m^{-2}). The insets in Fig. b and c, highlight the magnetophoretic effect. Pictures on the right correspond to the optical microscopy images of worn surfaces observed at the end of the test. The flow enters from the top. 10 × .

experiment. The friction level is low at all times, which is quite explainable when considering the PTFE molecular structure. The rigid, rod-like, [-(CF_2 – CF_2)-] chains orient on the counter-face surface during sliding and create a low shear strength coherent transfer film [44–46]. There is an initial overshot that disappears after 5 min, as already observed by Khedkar et al. [47]. Such a low friction value is in good agreement with XPS analyses on the worn surfaces that reveal an atomic concentration of fluor of 0.53% in the contact. This is more than three times larger than the concentration out of the contact region.

For the 5 and 9 rpm sliding speeds, the friction is roughly larger by a factor of 2 and do not vary much with time, contrary to the 1 rpm case. This larger friction is in agreement with the entrainment of PTFE particles into the contact [47,48].

The images of the steel plate surfaces after the tests are displayed on

the right hand side of Fig. 10 and quantitative image analysis has been performed to measure the wear-scar diameters and surface roughnesses in and out the point contact. The results are reported in Table 2. Significant differences in the wear-scars between the three sliding velocities are detectable for this 4.4 wt% PTFE-based IFF sample. The wear-scar diameter at 1 rpm (362 ± 8 μm) is clearly smaller than the wear-scar diameter at 5 rpm (463 ± 3 μm) and at 9 rpm (506 ± 9 μm). This is due to the fact that both the sliding distance and the rate of destruction of the film increases with the sliding speed.

6.2. Tribology with an applied magnetic field gradient in the point contact region

6.2.1. Optimization of the magnetic field gradient

By creating a magnetic field minimum in the point contact region, it is possible to apply locally a magnetophoretic force that will concentrate the non-magnetic lubricating particles contained in the IFF in that specific region. This necessitates combining several magnets.

In our experimental set-up, the small size of the steel plates has imposed the use of two small magnets only. On the one hand, their separation was fixed to $d = 3$ mm (see Fig. 1) so they could be embedded in the PLA matrix. On the other hand, their remanent magnetisation axes could be rotated to find the deepest field minimum at the point contact. Three configurations were evaluated where both magnets are aligned ($\hat{x}$, $\hat{y}$, $\hat{z}$) but pointing either in the same or in the opposite directions.

Fig. 11 displays the gradient of the magnetic field squared (normalized by the magnet remanent magnetisation squared) in the vicinity of the point contact (the yellow stripped square sketched in Fig. 1a) in cylindrical coordinates. The optimal configuration should have positive vertical and radial gradients components in order to drive the particles to the steel plate surface and concentrate them at the centre. Indeed, one recalls that the magnetophoretic force for IFFs is in opposite direction with respect to the gradient (see Eq. 4).

Unfortunately, it can be seen from Fig. 11 that a positive vertical component is not achievable with our set-up. Thus, our best choices are configurations with a nearly zero vertical component at the centre of the geometry: $(\hat{z}, \hat{z})$, $(\hat{z}, -\hat{z})$, $(\hat{x}, \hat{x})$ or $(\hat{y}, -\hat{y})$. The azimuthal component of the force has been analysed at the central point, looking for "stable" regions where the particle, if displaced, would return to its original position. Such regions are highlighted with a dotted line on the azimuthal component plot and particles are expected to concentrate along these lines. The $(\hat{y}, -\hat{y})$ configuration has the unique advantage to offer two stable lines for the azimuthal component, and a positive radial component at the centre. Therefore, the action of both the azimuthal and radial forces tends to focus the lubricants on the point contact. All friction experiments described in Figs. 10 and 12 have been performed in this particular configuration.

Strictly speaking, the configuration $(\hat{y}, \hat{y})$ also shares this advantage. However, it was not chosen because the radial force for this configuration does not have azimuthal symmetry and has a larger z-component than $(\hat{y}, -\hat{y})$.

Table 2
Root mean square (R_q) roughness for steel surfaces lubricated with a 4.4 wt% PTFE-based IFF after the friction test at different velocities (Fig. 10). Before observation, the surfaces were subjected to acetone treatment. Two regions were visualized: in the contact and out of the contact.

Sliding speed	Magnetic field	Wear-scar diameter (μm)	R_q (out of the contact region) (μm)	R_q (in the contact region) (μm)
1 rpm	w/o	362 ± 8	0.61 ± 0.03	0.76 ± 0.07
	w/	361 ± 5	0.51 ± 0.04	0.79 ± 0.04
5 rpm	w/o	463 ± 3	0.59 ± 0.03	1.05 ± 0.04
	w/	435 ± 6	0.59 ± 0.07	0.92 ± 0.01
9 rpm	w/o	506 ± 9	0.53 ± 0.03	0.99 ± 0.04
	w/	483 ± 1	0.56 ± 0.05	0.95 ± 0.09

According to our Finite Element Method simulations, the magnetic field at the point contact in the configuration $(\hat{y}, -\hat{y})$ has the following characteristics $H = 180$ A·m^{-1}; $\nabla H^2 = 10^9$ A^2·m^{-3} and $\nabla H = 2.6 \times 10^6$ A·m^{-2}. More detailed information can be found in the Supplementary Material file.

6.2.2. Friction under the optimized magnetic field gradient

Fig. 10a to c allows comparing the friction results for 4.4 wt% PTFE-based IFF suspensions at 3 different sliding speeds in presence or in absence of the magnetic field gradient created by the optimal configuration $(\hat{y}, -\hat{y})$. It is somewhat of a surprise that it is only at the intermediate sliding speed of 5 rpm that the application of a field gradient reduces the friction by 12% at long times. This result can, however, be understood as follows: if the velocity is too slow, the particles are not sufficiently entrained into the contact by the field to overcome Brownian diffusion (Fig. 10a). If the velocity is too fast, hydrodynamic forces govern and the particles cannot be trapped by the magnetophoretic force (Fig. 10c).

Fig. 12a and b displays the friction curves at the same particular speed of 5 rpm for the IFFs loaded with MoS_2 and SiO_2 particles, respectively. The curves for the PAO and FF carrier fluids are also given for reference. One readily observes that the magnetic field effect on the friction level is strikingly different for MoS_2 and SiO_2 particles than for PTFE particles. It is only in the case of PTFE that the friction is reduced when the field is turned on. The rationale for this behaviour is the difference in size of the particles: the smaller MoS_2 and SiO_2 particles are submitted to smaller magnetophoretic forces.

All in all, sufficiently large particles are needed for magnetophoretic forces to bring particles to the point contact and, hence, act as lubricants. If those particles are small, regardless their nature/chemistry, they will not reach the contact point in the sufficient amount and no significant effects on lubrication performance will be seen. Obviously, a definitive proof to corroborate this explanation would consist in repeating these tests with PTFE particles of different volume but with the same chemistry and morphology. In this way, the differences would be attributed only to the magnetophoretic force. We have not found such particles commercially available. Thus, this approximation would also imply developing a suitable synthesis route to get PTFE particles with a well-controlled shape and size. This is out of the scope of the present manuscript, where we just want to highlight the feasibility of IFFs as smart lubricants, and is proposed as a topic for future works.

The nature itself of the particles must of course be considered when discussing the lubricating properties of the various dispersions. On Fig. 12a and b, one can detect differences in the friction coefficient between MoS_2 and SiO_2 particles. MoS_2 particles reduce friction by roughly 8–11% when compared to FF, while SiO_2 particles increase it by 1–3%. This is not a surprise since MoS_2 particles are effectively known as better solid lubricants than SiO_2.

Finally, we have compared in Table 3 the extent of the damages caused to the steel surfaces by all suspensions (plus PAO) with and without a magnetic field gradient, after the friction tests of Figs. 10b -12a -b. The data are restricted to the sliding speed of 5 rpm since it is the only one that gives a friction reduction for the PTFE-based IFF sample when a field gradient is applied. The usual three characteristic parameters are reported, namely the wear scar diameter, and the surface roughness both in and out of the point contact. One can note immediately, that the surface roughnesses, R_q, out of the contact region are systematically lower than those in the contact region. Since this is quite understandable, they will not be discussed further.

For the MoS_2 and SiO_2 lubricating particles, no relevant changes are observed in the wear-scar diameters with and without magnetic field. This agrees with the fact that the field has no detectable influence on the friction coefficient. Their wear scars values are identical to each other within experimental accuracy, and similar to the wear scar produced by the FF suspension. These supposedly lubricating suspensions do not

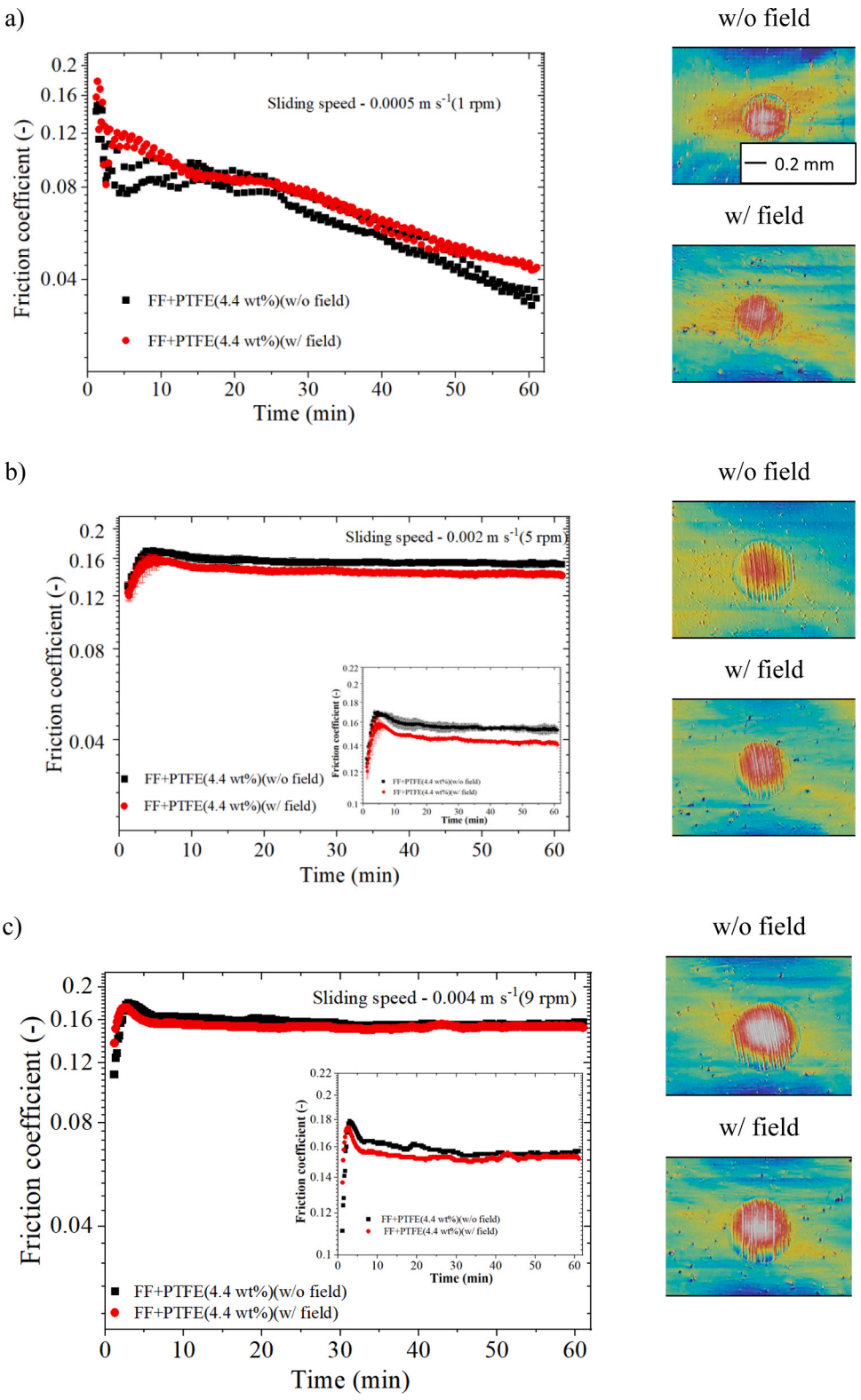

Fig. 11. Gradient of the magnetic field squared (normalized by the magnet magnetisation squared) around the point contact as a function of the relative orientation of the magnets for a magnet separation $d = 3$ mm. Red (blue) color stands for positive (negative) values of the gradient. The dotted lines in the azimuthal component correspond to the stable regions. The sizes of the squares are 3.5 mm × 3.5 mm. Coordinate system points to the positive directions. (For interpretation of the references to colour in this figure legend, the reader is referred to the web version of this article.)

improve the wear-out of the steel surfaces. The roughness R_q, in the contact region, seems larger for SiO_2 particles (1.13–1.15 μm) than for MoS_2 (0.67−1.13 μm), which is in line with their respective Mohs scale ratings of 4.5–6.5 in one case and 1–1.5 in the other. When the former nanoparticles plough the surface under the applied load, it accelerates the abrasion during friction, showing a worse anti-wear property [49].

For the PTFE particle, the field gradient induces a significant reduction in the wear scar diameter (measurements have been made in triplicate), again in agreement with the lowering of the friction coefficient observed when the field gradient is turned on. This is also in agreement with XPS analyses demonstrating a larger concentration of fluor when the field is applied in the 4.4 wt% PTFE-based IFF sample; an atomic concentration of fluor of 0.29% is measured in the contact in the absence of a magnetic field while a concentration of 0.34% is measured

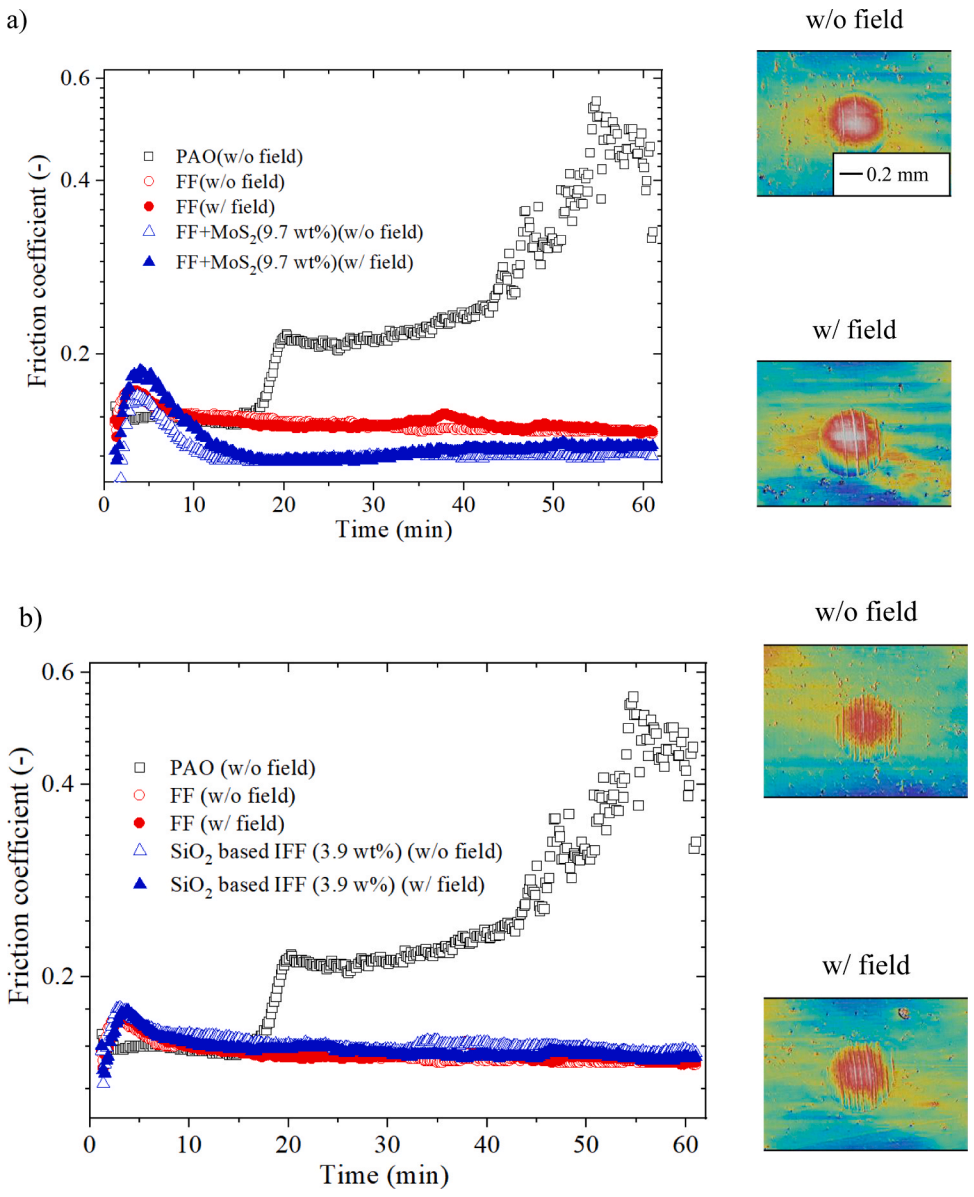

Fig. 12. Friction coefficient, μ, as a function of time, t, at a slow constant sliding speed $V = 5$ rpm $= 0.002$ m s^{-1} for MoS_2-based IFF (a-triangles) and SiO_2-based IFF (b-triangles). Particle concentration 9.7 wt% and 3.9 wt%, respectively. $F_N = 10$ N. As a reference we also include the friction data for the corresponding FF without nanoparticles (circles) and PAO (squares). Open points: without field. Solid points: with field. Pictures on the right correspond to the optical microscopy images of worn surfaces observed at the end of the test. The flow enters from the top. 10 × .

Table 3
Root mean square (R_q) roughness for steel surfaces lubricated with PAO, FF and 9.7 wt% MoS_2 and 3.9 wt% SiO_2 IFFs (i.e., concentration of 2 vol% in both cases) after the time dependent test (Fig. 12). Sliding speed = 5 rpm. Before observation, the surfaces were subjected to acetone treatment. Two regions were visualized in the contact and out of the contact.

Lubricant	Magnetic field	Wear-scar diameter (μm)	R_q (out of the contact region) (μm)	R_q (in the contact region) (μm)
PAO	w/o	532 ± 14	0.46 ± 0.02	2.61 ± 0.11
FF	w/o	463 ± 6	0.53 ± 0.08	1.02 ± 0.40
MoS_2-based IFF	w/o	460 ± 5	0.51 ± 0.04	0.67 ± 0.03
	w/	472 ± 7	0.53 ± 0.03	1.13 ± 0.03
SiO_2-based IFF	w/o	464 ± 12	0.73 ± 0.16	1.13 ± 0.08
	w/	458 ± 8	0.94 ± 0.14	1.15 ± 0.07

under the presence of the magnetic field. The surface roughness R_q, in the contact region, however, is not modified. It is of the same order as for the other two lubricating particles and for FF. This tends to prove that the abrasion is primarily caused by the magnetite particles that are present in all FF and IFF suspensions.

Even though PAO contains neither abrasive particles nor lubricating particles, the damages caused to the steel surfaces are much higher. Wear scar diameter is larger by 15% and roughness more than doubles. The friction coefficient is by far the highest measured in Fig. 12 and increases continuously during the 60 min run time of the experiment. IFF and FF suspensions are clearly better lubricants than PAO.

7. Conclusions

We show that inverse ferrofluids formulated with solid nano-lubricants could be a solution to control friction in narrow spaces such as point contacts. The approach requires creating a magnetic field gradient in the region that needs to be lubricated. This gradient has been generated by combining the fields of two permanent magnets. Our results have been obtained for three different nano-lubricants (PTFE, MoS_2 and SiO_2), and at several sliding speeds. They show that friction reduction by the magnetic field gradient requires several conditions: the particles should be large enough for the magnetophoretic effect to apply (PTFE is better than MoS_2 and SiO_2 in our experiments), and the sliding speed should be in the appropriate range (not too small and not too

large) for allowing the lubricating particles to feed the gap.

CRediT authorship contribution statement

Rasmita Sahoo: Investigation, Validation, Writing – original draft. **Paula Ussa-Aldana:** Methodology, Resources, Supervision. **Denis Lancon:** Resources. **Francis Rondelez:** Resources, Writing – review & editing. **Jose R. Morillas:** Methodology, Investigation, Software, Writing – review & editing. **Roque Hidalgo-Alvarez:** Methodology, Writing – review & editing. **Juan de Vicente:** Conceptualization, Methodology, Writing – review & editing, Supervision, Project administration, Funding acquisition.

Declaration of Competing Interest

The authors declare that they have no known competing financial interests or personal relationships that could have appeared to influence the work reported in this paper.

Acknowledgements

We acknowledge F. Vereda for his help in the laboratory during the synthesis of magnetite particles. This work was supported by Total Marketing Services. J. de Vicente and R. Hidalgo-Alvarez acknowledge MICINN PID2019–104883GB-I00 project, Junta de Andalucía P18-FR-2465 project and European Regional Development Fund (ERDF). J. R. Morillas acknowledges FPU14/01576 fellowship. Funding for open access charge by Universidad de Granada / CBUA is acknowledged.

Appendix A. Supporting information

Supplementary data associated with this article can be found in the online version at doi:10.1016/j.triboint.2021.107346.

References

[1] Zhao J, Huang Y, He Y, Shi Y. Nanolubricant additives: a review. Friction 2021;9:891–917.
[2] Kotia A, Rajkhowa P, Rao GS, Ghosh SK. Thermophysical and tribological properties of nanolubricants: a review. Heat Mass Transf 2018;54:3493–508.
[3] Shafi WK, Charoo MS. An overall review on the tribological, thermal and rheological properties of nanolubricants. Tribol Mater Surf Interfaces 2021;15:20–54.
[4] Salimi-Yasar H, Heris SZ, Shanbedi M. Influence of soluble oil-based TiO2 nanofluid on heat transfer performance of cutting fluid. Tribol Int 2017;112:147–54.
[5] Mousavi SB, Heris SZ, Estellé P. Experimental comparison between ZnO and MoS_2 nanoparticles as additives on performance of diesel oil-based nano lubricant. Sci Rep 2020;10:1–17.
[6] Nabil MF, Azmi WH, Hamid KA, Zawawi NNM, Priyandoko G, Mamat R. Thermophysical properties of hybrid nanofluids and hybrid nanolubricants: a comprehensive review on performance. Int Commun Heat Mass Transf 2017;83:30–9.
[7] Azman NF, Samion S. Dispersion stability and lubrication mechanism of nanolubricants: a review. Int J Precis Eng Manuf -Green Tech 2019;6:393–414.
[8] Kumar S, Sehgal R, Wani MF, Sharma MD. Stabilization and tribological properties of magnetorheological (MR) fluids: a review. J Magn Magn Mater 2021;538:168295.
[9] Morillas JR, de Vicente J. Magnetorheology: a review. Soft Matter 2020;16:9614–42.
[10] Chin BD, Park JH, Kwon MH. Rheological properties and dispersion stability of magnetorheological suspensions. Rheol Acta 2001;40:211–9.
[11] Rich JP, Doyle PS, McKinley GH. Magnetorheology in an aging, yield stress matrix fluid. Rheol Acta 2012;51:579–93.
[12] Shan L, Jia W, Zhou M, Meng Y, Zhang X, Tian Y. Frequency-independent viscoelasticity of carbonyl iron particle suspensions under a magnetic field. Smart Mater Struct 2017;26:054009.
[13] Shahrivar K, de Vicente J. Ferrofluid lubrication of compliant polymeric contacts: effect of non-homogeneous magnetic fields. Trib Lett 2014;56:281–92.
[14] Shahrivar K, Ortiz AL, de Vicente J. A comparative study of the tribological performance of ferrofluids and magnetorheological fluids within steel-steel point contacts. Trib Int 2014;78:125–33.
[15] Bombard AJF, Gonçalves FR, Shahrivar K, Ortiz AL, de Vicente J. Tribological behavior of ionic liquid-based magnetorheological fluids in steel and polymeric point contacts. Trib Int 2015;81:309–20.
[16] Zhang P, Lee KH, Lee CH. Friction characteristics of magneto-rheological fluid on DLC- and PTFE-coated surfaces. J Eng Trib 2017;231:1–9.
[17] Rosa WO, Vereda F, de Vicente J. Tribological behavior of glycerol/water-based magnetorheological fluids in PMMA point contacts. Front Mater 2019;6:32.
[18] Felicia LJ, Vinod S, Philip J. Recent advances in magnetorheology of ferrofluids (magnetic nanofluids)—a critical review. J Nanofluids 2016;5:1–22.
[19] Andablo-Reyes EA, Hidalgo-Alvarez R, de Vicente J. Controlling friction using magnetic nanofluids. Soft Matter 2011;7:880–3.
[20] Shi X, Huang W, Wang X. Ionic liquids–based magnetic nanofluids as lubricants. Lubr Sci 2018;30:73–82.
[21] Skjeltorp AT. One- and two-dimensional crystallization of magnetic holes. Phys Rev Lett 1983;51:2306–9.
[22] de Gans BJ, Duin NJ, den Ende DV, Mellema J. The influence of particle size on the magnetorheological properties of an inverse ferrofluid. J Chem Phys 2000;113:2032–42.
[23] Saldivar-Guerrero R, Richter R, Rehberg I, Aksel N, Heymann L, Rodriguez-Fernandez OS. Solid to liquid transition of inverse ferrofluids under shear. Magnetohydrodynamics 2005;41:385–9.
[24] de Gans BJ, Blom C, Mellema J, Philipse AP. Preparation and magnetisation of a silica-magnetite inverse ferrofluid. J Mag Mag Mat 1999;201:11–3.
[25] Saldivar-Guerrero R, Richter R, Rehberg I, Aksel N, Heymann L, Rodriguez-Fernandez OS. Viscoelasticity of mono- and polydisperse inverse ferrofluids. J Chem Phys 2006;125:084907.
[26] Ramos J, Klingenberg DJ, Hidalgo-Álvarez R, de Vicente J. Steady shear magnetorheology of inverse ferrofluids. J Rheol 2011;55:127–52.
[27] Ekwebelam CC, See H. Determining the flow curves for an inverse ferrofluid. Korea-Aust Rheol J 2008;20:35–42.
[28] Ruiz-López JA, Fernández-Toledano JC, Klingenberg DJ, Hidalgo-Alvarez R, de Vicente J. Model magnetorheology: A direct comparative study between theories, particle-level simulations and experiments, in steady and dynamic oscillatory shear. J Rheol 2016;60:61–74.
[29] Ruiz-López JA, Hidalgo-Alvarez R, de Vicente J. Towards a universal master curve in magnetorheology. Smart Mater Struct 2017;26:054001.
[30] Sherman SG, Becnel AC, Wereley NM. Relating Mason number to Bingham number in magnetorheological fluids. J Mag Mag Mat 2015;380:98–104.
[31] Sherman SG, Powell LA, Becnel AC, Wereley NM. Scaling temperature dependent rheology of magnetorheological fluids. J Appl Phys 2015;117:17C751.
[32] Susan-Resiga D, Vekas L. Ferrofluid based composite fluids: magnetorheological properties correlated by Mason and Casson numbers. J Rheol 2017;61:401–8.
[33] Klingenberg DJ, Ulicny JC, Golden MA. Mason numbers for magnetorheology. J Rheol 2007;51:883–93.
[34] Berli CLA, de Vicente J. A structural viscosity model for magnetorheology. Appl Phys Lett 2012;101:021903.
[35] Stöber W, Fink A. Controlled growth of monodisperse silica spheres in the micron size range. J Colloid Interface Sci 1968;26:62–9.
[36] Massart R. Preparation of aqueous magnetic liquids in alkaline and acidic media. IEEE Trans Magn 1981;17:1247–8.
[37] Charles SW. The preparation of magnetic fluids. In: Odenbach S, editor. Ferrofluids. Bremen, Germany: Springer; 2002. p. 6–9.
[38] Laun HM, Schmidt G, Gabriel C, Kieburg C. Reliable plate–plate MRF magnetorheometry based on validated radial magnetic flux density profile simulations. Rheol Acta 2008;47:1049–59.
[39] Odenbach S. Ferrofluids. In: Buschow KHJ, editor. Handbook of Magnetic Materials. vol. 16. Elsevier; 2006.
[40] Jönkkäri I, Syrjälä S. Evaluation of techniques for measuring the yield stress of a magnetorheological fluid. Appl Rheol 2010;20:45875.
[41] Yang Y, Li L, Chen G. Static yield stress of ferrofluid-based magnetorheological fluids. Rheol Acta 2009;48:457–66.
[42] Bonnecaze RT, Brady JF. Yield stresses in electrorheological fluids. J Rheol 1992;36:73–115.
[43] Tannous J, Dassenoy F, Lahouij I, Mogne TL, Vacher B, Bruhacs A, et al. Understanding the tribochemical mechanisms of IF-MoS2 nanoparticles under boundary lubrication. Tribol Lett 2011;41:55–64.
[44] Blanchet TA, Peng YL, Nablo SV. Tribology of selectively irradiated PTFE surfaces. Tribol Lett 1998;4:87–94.
[45] Conte M, Igartua A. Study of PTFE composites tribological behaviour. Wear 2012;296:568–74.
[46] Davim JP. Tribology of nanocomposites. Springer; 2013.
[47] Khedkar J, Negulescu I, Meletis EI. Sliding wear behavior of PTFE composites. Wear 2002;252:361–9.
[48] Tanaka K, Uchiyama Y, Toyooka S. The mechanism of wear of polytetrafluoroethylene. Wear 1973;23:153–72.
[49] Xie H, Jiang B, He J, Xia X, Pan F. Lubrication performance of MoS_2 nd SiO_2 nanoparticles as lubricant additives in magnesium alloy-steel contacts. Tribol Int 2016;93:63–70.